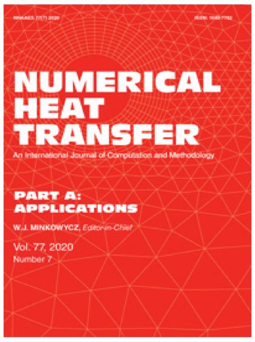

Numerical Heat Transfer, Part A: Applications

An International Journal of Computation and Methodology

ISSN: 1040-7782 (Print) 1521-0634 (Online) Journal homepage: https://www.tandfonline.com/loi/unht20

Thermal performance and flow characteristics of two-phase loop thermosyphons

Sara Kloczko & Amir Faghri

To cite this article: Sara Kloczko & Amir Faghri (2020) Thermal performance and flow characteristics of two-phase loop thermosyphons, Numerical Heat Transfer, Part A: Applications, 77:7, 683-701, DOI: 10.1080/10407782.2020.1714342

To link to this article: https://doi.org/10.1080/10407782.2020.1714342

NUMERICAL HEAT TRANSFER, PART A: APPLICATIONS
2020, VOL. 77, NO. 7, 683–701
https://doi.org/10.1080/10407782.2020.1714342

Thermal performance and flow characteristics of two-phase loop thermosyphons

Sara Kloczko and Amir Faghri

Department of Mechanical Engineering, University of Connecticut, Storrs, USA

ABSTRACT

A detailed 2-D computational fluid dynamics (CFD) model simulating two-phase flow and heat transfer in a two-phase loop thermosyphon (TPLTS) is presented. The CFD simulation was built to represent two-phase flow and heat transfer phenomena during the transient and steady-state operation analysis of a TPLTS under various operating conditions. The two-phase flow was modeled using the volume of fluid (VOF) model, and the Lee model was utilized for evaporation and condensation. Simulation results were compared with experimental temperature, pressure, and flow visualization data.

ARTICLE HISTORY
Received 5 October 2019
Accepted 5 January 2020

1. Introduction

A heat pipe is a highly effective and well-established device which transfers a large amount of heat from one location to another. The components of a conventional heat pipe are the wick, outer wall, and working fluid, which flows through the three main sections of the heat pipe: evaporator, adiabatic section, and condenser [1]. A diagram of a conventional heat pipe is shown in Figure 1*a* [2]. There is a small temperature drop between the evaporator and condenser section of the heat pipe, referred to as the adiabatic section, where the heat pipe operates nearly isothermally [3]. Heat is applied externally to the evaporator section and vaporizes the fluid in the saturated wick, which is driven by the vapor pressure through the adiabatic section to the condenser where it condenses and releases its latent heat, then is returned to the evaporator by capillary action of the wick [4,5]. The main driver of heat transfer in the conventional heat pipe is phase change and the wick. There are several different types of heat pipe depending on the application, including: conventional heat pipes, loop heat pipes (LHP), pulsating heat pipes (PHP), and thermosyphons, which can also be broken up into conventional thermosyphons and single- and two-phase loop thermosyphons (TPLTSs). A conventional heat pipe reliant on phase change has several limits. These limits include the viscous, sonic, capillary, entrainment, flooding, and boiling limits. Challenges and opportunities of heat pipes are discussed by Faghri [6]. Heat pipe analysis and numerical simulation covering all types of heat pipes with various levels of approximation are reviewed by Bergman and Faghri [7].

A two-phase conventional thermosyphon (TPCTS), a schematic of which is shown in Figure 1*b*, is sometimes referred to as gravity assisted heat pipe and consists of an evaporator and condenser. There is no wick in a TPCTS because the force of gravity drives the fluid flow. The liquid and vapor occupy a single straight tube and the flow is counter-current. The heat input to the evaporator vaporizes the working fluid, which then flows up to the condenser. The working fluid

CONTACT Sara Kloczko Sara.Kloczko@Uconn.edu Department of Mechanical Engineering, University of Connecticut, 191 Auditorium Road, Storrs, CT 06269-3139, USA.

Nomenclature

A_c	cross-sectional area (m^2)
A_s	surface area (m^2)
D	diameter (m)
h	convection coefficient (W/ m^2·co
h	specific enthalpy (J/kg)
$\sim h$	average enthalpy of multiphase mixture (J/kg)
k	thermal conductivity (W/m·K)
L	length (m)
$\dot{m}$	rate of mass transfer due to evaporation or condensation (kg/s·m^3)
$\dot{m}\,'''_{jk}$	mass transfer per unit volume from phase j to phase k due to phase change
$\dot{\mathbf{M}}'''_I$	momentum production rate due to interaction between phases along their separating interfaces $\dot{\mathbf{M}}'''_I = \sum_{k=1}^{\Pi} \sum_{j=1(j\neq k)}^{\Pi} \left\langle \dot{m}\,'''_{jk} \right\rangle \langle \mathbf{V}_{k,I} \rangle^k$
p	pressure (Pa)
$\mathbf{q}''$	heat flux vector (W/m^2)
q'''	internal heat generation per unit volume (W/m^3)
$\dot{Q}$	heat (W)
r	mass transfer intensity factor
T	temperature (K)
$\mathbf{V}$	velocity vector (m/s)
$\sim \mathbf{V}$	mass-averaged velocity vector, $\frac{1}{\langle \rho \rangle} \left(\sum_{k=1}^{\Pi} \varepsilon_k \langle \rho_k \rangle^k \langle \mathbf{V}_k \rangle^k \right)$ (m/s)
$\mathbf{X}$	body force vector

Greek Symbols

ε	volume fraction
Π	number of phases
ρ	density (kg/m^3)
$\boldsymbol{\tau}$	viscous stress tensor (N/m^2)
$\boldsymbol{\tau}'$	stress tensor (N/m^2)
∇	laplace operator vector

Subscript

a	adiabatic
ave	average
c	condenser
e	evaporator
eff	effective
I	interface
in	input
kk^{th}	phase
l	liquid phase
max	maximum
out	output
r	radial
sat	saturated state
v	vapor phase
∞	free stream

Other

$\langle\ \rangle$	volume averaged
$\langle\ \rangle^{k}$	phase averaged
$\frac{D}{Dt}$	substantial derivative

is then condensed back into a liquid in the condenser section, releases its latent heat, and drains back down the walls to the evaporator.

Due to the counter-current flow of the liquid and vapor, the thermosyphon performance is limited by the flooding limit. This occurs when working fluid temperature is low, and vapor velocity is high. The shear of the vapor traveling to the condenser prevents liquid film on the wall from traveling back to the condenser. The conventional thermosyphon is also subject to the dry-out limit. This occurs when the fill charge ratio is too small and the condensate film eventually dries out [8].

There are two main approaches for full numerical simulation of two-phase, closed, wickless thermosyphons. The first is the separated model approach, where a set of localized governing equations for mass, momentum, and energy conservation are solved separately for the liquid and vapor phases. Harley and Faghri [9] developed a steady and transient two-dimensional thermosyphon separated flow model which accounts for conjugate heat transfer through the wall and the falling condensate film. The model was extended by Shabgard et al. [10] to include various filling conditions of the thermosyphon. The second approach uses the multifluid–Eulerian model which allows liquid-vapor penetration and requires volume averaging to be performed on the governing equations [1, 11].

Many numerical simulations have been performed to understand the two-phase flow in the TPCTS and the effects of varying several parameters on the overall performance. Wang et al. [12] conducted a combined CFD and experimental flow visualization investigation. They used the

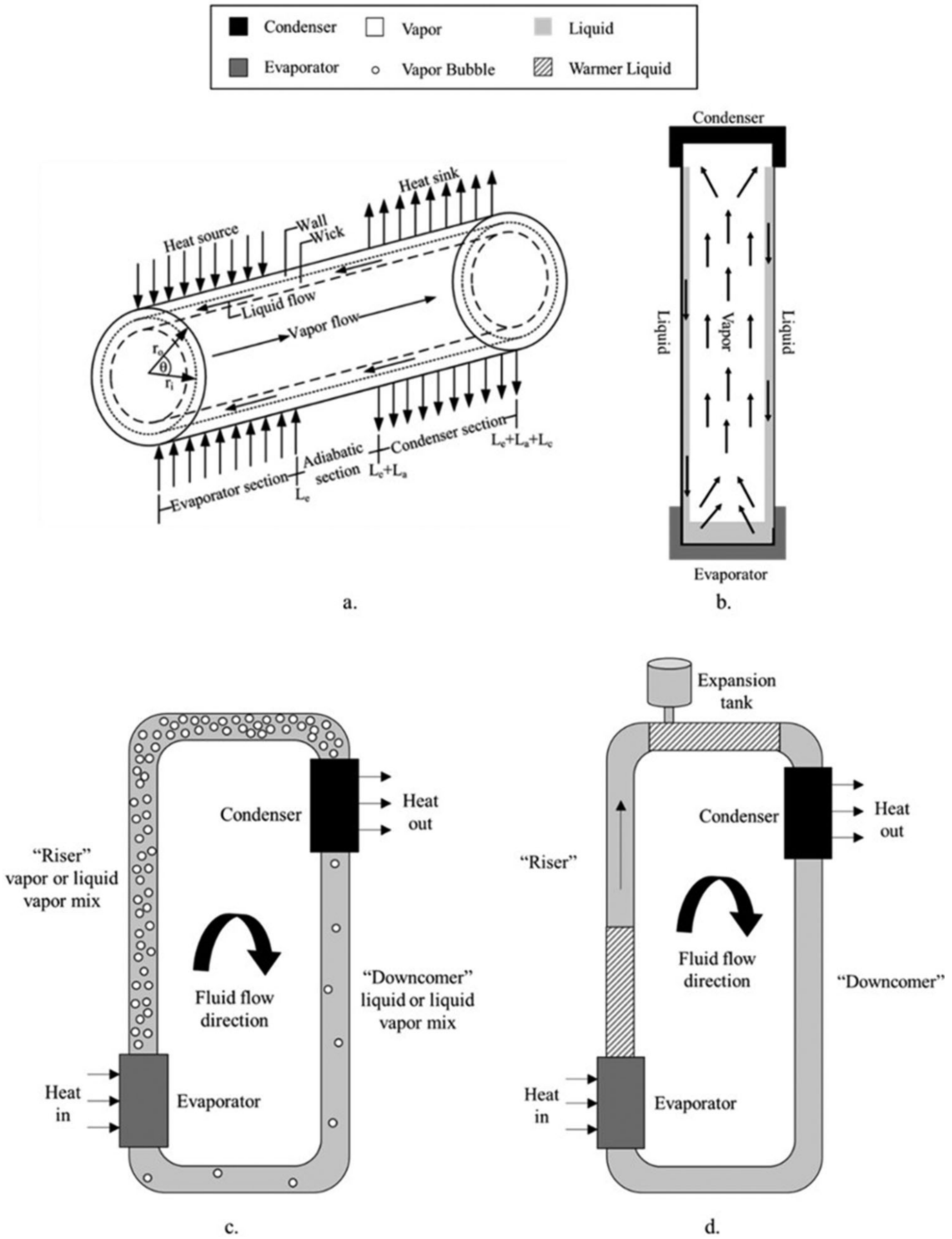

Figure 1. Diagrams of (a) conventional heat pipe, (b) two-phase conventional thermosyphon, (c) two-phase loop thermosyphon, and (d) single-phase loop thermosyphon showing the flow of liquid and/or vapor.

VOF method for modeling two-phase flow, and both the Lee model and an improved Lee model that considers superheat to increase prediction performance. The authors concluded that the bubble growth behavior is much more accurate to the experiment when using the improved Lee model than the original. However, though the improved Lee model was able to better reproduce the bubble expulsion phenomenon, the bubble growth rate was much different in the simulation than in the experiment. Alizadehdakhel et al. [13] and Fadhl et al. [14] developed models to simulate two-phase heat transfer through a TPCTS. Both used ANSYS to create their models and the VOF model and user-defined functions (UDFs) to model the multiphase flow and evaporation-condensation of the working fluid. Jouhara et al. [15] developed a 3-D CFD model using the VOF method and UDFs which also included the cooling fluid in the condenser as part of the model. Xu et al. [16] developed a model using VOF and a UDF to model phase change and simulate heat transfer characteristics in a TPCTS. They also investigated the effects of changing the transient mass transfer time relaxation parameter on the temperature and performance results. Naresh and Balaji [17] developed a thermal circuit model to study the flow and heat transfer processes in an internally finned two-phase thermosyphon, with results within 5% of experimental data. Zou and Wang [18] developed a mathematical model that can successfully reproduce the complex flow characteristic and heat transfer inside a TPCTS, including the distributions of liquid film, velocity with vapor-liquid based on the Nusselt model.

The TPLTS, a general schematic of which is shown in Figure 1*c*, consists of an evaporator, riser, condenser, and downcomer. Heat input to the evaporator section vaporizes the working fluid [19]. The vapor (or liquid-vapor mix, depending on the initial fill ratio) then flows up the riser to the condenser where it is condensed back into a liquid. The flow in the TPLTS is co-current, with liquid and vapor flowing in the same direction around the loop. The liquid phase (or liquid-vapor mix, depending on the initial fill ratio) flows down the downcomer back to the evaporator. The flow of liquid is driven by the density difference of the lower temperature fluid coming from the condenser and the higher temperature lower density flow from the evaporator [20]. The TPLTS has no flooding limit. Some TPLTS have wicks in the evaporator and some do not. However, the TPLTS operates more effectively with wick structures in the evaporator than without [21]. The TPLTS relies on gravity for the flow of working fluid and the heat transfer relies on the heat of vaporization.

Several attempts have been made at modeling TPLTS. Dobson and Ruppersberg [22] conducted theoretical simulations for single-phase and TPLTSs with expansion tanks, and TPLTSs without expansion tanks. Their theoretical results were able to capture single and two-phase flow with expansion tanks well, but were not able to capture the operating modes in the two-phase without expansion tank model. Park et al. [23] developed a 2-D CFD model using Fluent to analyze two-phase flow through a loop thermosyphon as a defrost device in a refrigerator. They modeled the flow of the working fluid as turbulent, using the k-ω model. Zhang et al. [24] developed a generalized model for a TPLTS using conservation equations of momentum, energy, and mass simultaneously, where the downcomer can be either partially or fully filled with liquid. Their model was able to simulate the behavior of a TPLTS under small temperature difference. Aung and Li [25] used a MATLAB program for the iterative solution of flow through a two-phase closed-loop thermosyphon with varying riser diameter and inclination angle. Bodjona et al. [26] conducted a numerical investigation of a TPLTS in steady and transient states by creating a 1-D flow model which considers subcooled liquid and overheated vapor as well as evaporation and condensation. A specific hyperbolic solver based on Godunov method and Harten-Lax-van Leer-Contact (HLLC) Riemann solver was used to solve the model simulations. Bodjona et al. [27] later developed 1-D reduced models, built using the Modal Identification Method, to simulate the behavior of a TPLTS which requires much less CPU time than typical 2-D or 3-D simulations.

The third type of thermosyphon is the single-phase loop thermosyphon (SPLTS) which is also sometimes referred to as single-phase natural circulation loop, a general schematic of which is shown in Figure 1*d*. The basic structure is the same as that of a TPLTS with an evaporator section which heats the working fluid, a pipe connecting the evaporator to the condenser (riser), a condenser which cools the working fluid, and another pipe connecting the condenser to the evaporator (downcomer) through which the working fluid flows back to the evaporator. The flow is driven by the hydrostatic pressure difference that results from the temperature gradient and resulting density gradient from the evaporator to the condenser. Fluid motion is generated by density differences in the working fluid due to temperature gradients generated by the evaporator and condenser [28]. The motion is governed by the balance of the opposite effects of buoyancy (due to the different fluid densities in the ascending (warm) and descending (cold) sections), and friction [29]. Generally, the heat sink is above the heat source to enhance the circulation rates [30]. A disadvantage of the SPLTS is that interaction between buoyancy and frictional forces can be unstable. There is also an expansion tank shown in Figure 1*d*, which may be present in a SPLTS to accommodate the volume expansion of working fluid as temperature increases.

Various studies have investigated flow and heat transfer simulation of SPLTS. Maiani et al. [29] created an analytical model describing the system and obtained a parametric representation of the behavior of a SPLTS assuming more general correlations for friction factor and heat transfer coefficient than are generally used. They studied the stability of the system by linearizing momentum and energy conditions and applying a first-order perturbation method. Burroughs et al. [31] modeled a SPLTS with the heat source on the bottom and used the Navier–Stokes equations and the boussinesq approximation to derive a model where the first Fourier modes decouple leaving a system of three coupled nonlinear PDEs that completely describe the flow. They compared the predictions of their reduced model with numerical simulations of the 3-D Navier–Stokes equations and the boussinesq approximation and found good agreement around the onset of convection. Pilkhwal et al. [32] used 1-D and 3-D CFD codes to predict behavior observed in the experiments of a SPLTS. The code was effective in showing the origin of the pulsating instabilities that were seen in the experiment. Naveen et al. [33] created a 1-D model for simulating the startup of a single-phase loop thermosyphon using a pseudo-conductivity model which takes into account the energy transfer by local convection. Farawila et al. [34] developed an analytical solution to represent the basic instability mechanisms where a simple analog was constructed such that the analytical solutions were free from diffusion and damping problems that are present in finite volume analyses. Their model fits the idealized case of single-phase flow with a constant pressure drop boundary condition and a fixed heat source. They also developed an extension of the model for two-phase flow due to bulk boiling in the riser. Luzzi et al. [35] developed 1-D semi-analytical and 3-D numerical models to study the dynamic behavior of natural convection. Cheng et al. [36] developed a 3-D transient numerical simulation of a SPLTS. The transient response was obtained based in the finite difference method for solving 1-D momentum and energy equations. Bejjam and Kiran Kumar [37] created a 3-D model for simulating flow through a SPLTS using ANSYS Fluent and the mixture model to solve conservation equations.

While many numerical studies have been conducted for various types of thermosyphon, few numerical simulations have been created to model the TPLTS. Also, there is no systematic approach to observe flow patterns within a closed-loop two-phase thermosyphon. Furthermore, flow characteristics of a TPLTS have not been modeled in detail and compared to experimental results.

In this effort, a detailed transient 2-D CFD simulation was developed to model the heat transfer and flow visualization in a TPLTS. The VOF multiphase model was used to simulate flow and heat transfer characteristics for several working fluid fill ratios and heat inputs. Temperature and pressure response and flow patterns are also compared to experimental results discussed in previous works by the present authors [38].

2. Numerical methodology

The multi-fluid model is one method for the formulation of macroscopic equations of a multiphase system, obtained using phase averaging. The multi-fluid model performs averaging for each individual phase within a multiphase control volume [11]. In this computational model, one set of equations is generated for each phase present in the system. These equations describe the flow within the control volume. The mixture model is another method for the formulation of macroscopic equations of a multiphase system. In the mixture model, spatial averaging is performed over both phases simultaneously within the control volume, and the phases are considered together as a whole. Governing equations for the mixture model are obtained by adding the multi-fluid equations for each phase. Therefore, only one equation is solved for each conservation equation. The mixture model solves the momentum equation by describing the dispersed phases with relative velocities. The ANSYS Fluent VOF model ("Volume of Fluid (VOF) Model Theory," 2006) is used to model multiphase flow in the TPLTS and uses both multi-fluid and mixture models to describe the flow for this 2-D transient model [39]. The advantage of the VOF model is that the motion of the two-phase interface can be distinctly captured by the determination of phase interface [40].

In this approach, the multi-fluid model is used to solve the continuity equation; there is one equation for each phase present in the multiphase control volume. The following equation describes the continuity equation for the volume fraction of each phase to track the interface between phases [11]:

$$\frac{\partial}{\partial t}\left(\varepsilon_k\langle\rho_k\rangle^k\right)+\nabla\cdot\left(\varepsilon_k\langle\rho_k\rangle^k\langle\mathbf{V}_k\rangle^k\right)=\sum_{j=1(j\neq k)}^{\Pi}\left(\dot{m}_{jk}^{'''}\right). \tag{1}$$

Since the sum of the volume fractions of all the fluid phases present in each computational cell must sum to 1, volume fraction is solved for each phase except the primary phase, which is defined by ease of modeling to be the liquid phase working fluid. The volume fraction of the primary phase is determined by solving for the volume fraction such that the sum of all volume fractions is 1.

The mixture model is used to solve the momentum equation. A single momentum equation is solved throughout the domain, which is dependent on the volume fractions of all the phases. The properties in the momentum equation are calculated based on the phases in each control volume. The mixture model momentum equation is:

$$\frac{\partial}{\partial t}\left(\langle\rho\rangle\sim\mathbf{V}\right)+\nabla\cdot\sum_{k=1}^{\Pi}\varepsilon_k\langle\rho_k\rangle^{\mathrm{k}}\langle\mathbf{V}_k\mathbf{V}_k\rangle^{\mathrm{k}}=\ \nabla\cdot\langle\boldsymbol{\tau}'\rangle+\langle\rho\rangle\mathbf{X}+\dot{\mathbf{M}}_I^{'''}. \tag{2}$$

The energy equation, like the momentum equation, is shared among the phases and uses the mixture model. The mixture model energy equation is [11]:

$$\frac{\partial}{\partial t}\left(\langle\rho\rangle\sim h\right)+\nabla\cdot\left(\sum_{k=1}^{\Pi}\varepsilon_k\langle\rho_k\rangle^k\langle\mathbf{V}_k h_k\rangle^k\right)=-\nabla\cdot\left\langle\mathbf{q}^{''}\right\rangle+\frac{D\langle p\rangle}{Dt}+\left\langle q^{'''}\right\rangle+\nabla\sim\mathbf{V}:\langle\tau\rangle+q_I^{'''}. \tag{3}$$

The working fluid inside the TPLTS is R134a. The ideal gas law is used to model the density of the vapor phase. Other properties are modeled as functions of temperature with polynomial relations obtained using data from NIST ("Thermophysical Properties of Fluid Systems") [41]. The boussinesq approximation is applied for density of the liquid phase of R134a. Again, all other properties are defined as polynomial functions of temperature. The saturation temperature for R134a is defined as a function of saturation pressure. The saturation temperature and pressure are related using a polynomial relationship with properties obtained from NIST. The phase change is modeled using the Lee model [42]. The Lee model uses the following equations to calculate mass transfers:

$$\dot{m}_v=-\dot{m}_l=r_l\varepsilon_l\rho_l\frac{T-T_{sat}}{T_{sat}}\quad T>T_{sat}\ \text{(evaporation process)} \tag{4}$$

$$\dot{m}_l=-\dot{m}_v=r_v\varepsilon_v\rho_v\frac{T_{sat}-T}{T_{sat}}\quad T<T_{sat}\ \text{(condensation process)} \tag{5}$$

According to Sun et al. [43], the value of r is recommended to be such as to maintain the interfacial temperature reasonably close to the saturation temperature, and to avoid divergence

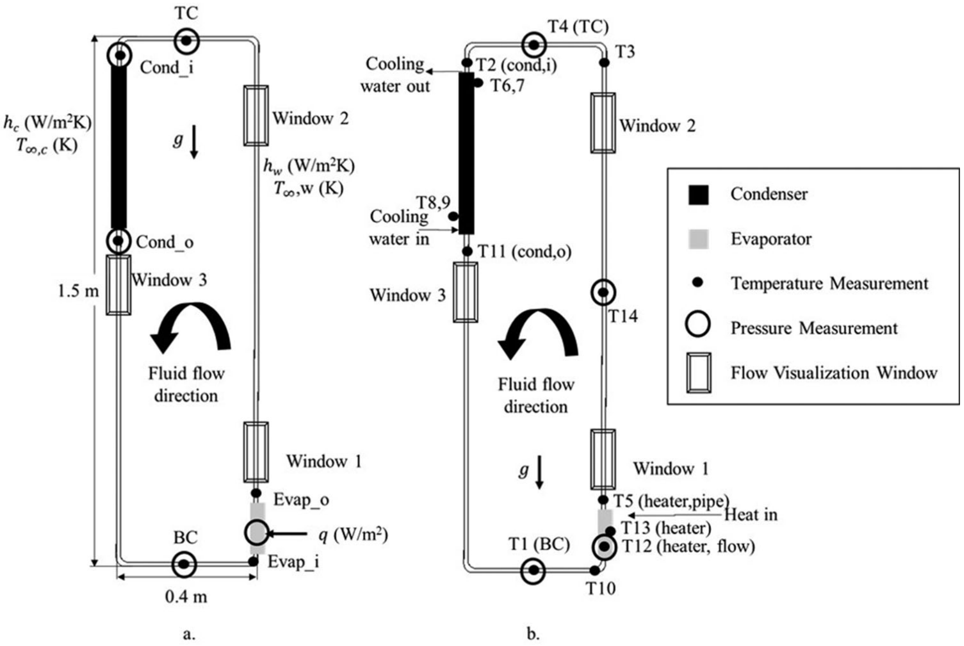

Figure 2. (a) Model geometry and dimensions and (b) diagram of experiment.

issues. Generally, r_l and r_v are set equal to 0.1 as the default in numerical analysis. However, in this simulation, r_l and r_v are set proportional to ρ_l and ρ_v through the equation:

$$r_l = r_v \frac{\rho_l}{\rho_v} \tag{6}$$

where r_v is set to 0.1. Consideration of the density ratio will maintain balance between the evaporating mass transfer and the condensing mass transfer during phase change [44]).

The continuum surface force model (CSF) is used to model surface tension [45]. The surface tension between the liquid and vapor phases of R134a is modeled using a polynomial relationship with temperature. The model described above is created in ANSYS Fluent.

Figure 2*a* shows the geometry and boundary conditions of the loop thermosyphon modeled in the simulation, and Figure 2*b* shows the diagram of the thermosyphon used in experiments. The loop is modeled as stainless steel with inner and outer diameters of 10.9 and 12.7 mm, respectively. A non-slip boundary condition is imposed on the inner walls of the TPLTS. The evaporator section is modeled as constant heat flux, the condenser is modeled as a convection boundary between the cooling water (not modeled) and the thermosyphon wall, and the remainder of the wall is modeled as a convection boundary to account for heat loss to the environment. The convection coefficients are obtained from experimental data. The following equation is used to calculate the convection coefficient between the condenser section of the pipe and the cooling water:

$$h_c = \frac{\dot{Q}_{out}}{\pi D L_c (T_{c,ave} - T_\infty)} \tag{7}$$

where T_∞ is the temperature of the cooling water. A similar equation is used to calculate the convection coefficient between the wall and the air, except $T_{c,ave}$ is replaced with the average loop temperature and T_∞ is the room temperature.

The system is divided into regions where each region is specified with initial conditions; a small fraction of the volume, usually 5–10%, is specified to have an R134a vapor volume fraction of 1, the remainder is saturated liquid R134a. The initial temperature and pressure of the

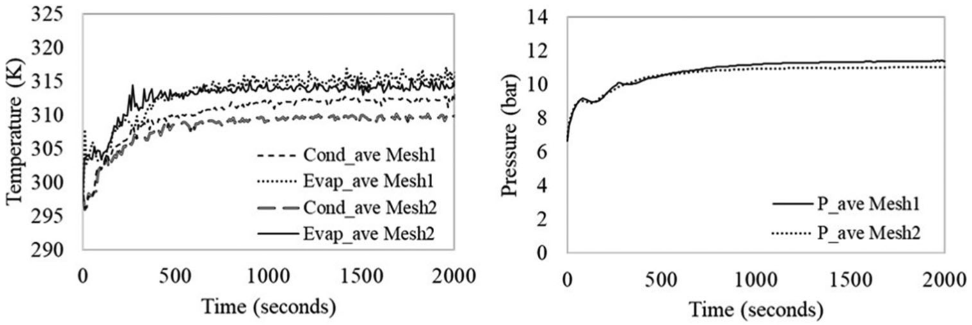

a. b.

Figure 3. (a) Simulation transient response for (a) temperature and (b) pressure for Mesh1 and Mesh2 for 90% R134a fill ratio and 200 W heat input simulation.

Table 1. Grid independence temperature and pressure comparison for 90% R134a fill ratio and 200 W heat input simulations.

Elements	Pressure (bar)	TC (K)	BC (K)	Evaporator (K)	Condenser (K)
40,909 (Mesh1)	11.39	314.90	312.31	315.39	312.31
85,104 (Mesh2)	11.02	313.00	308.90	314.17	309.63
% Difference	3.30	0.61	1.10	0.39	0.86

simulation are 298 K and 667,690 Pa, respectively, which are the saturation conditions at room temperature.

The temperature distribution along the wall of the TPLTS is measured at six locations in the model: just before and after the evaporator section (Evap_i and Evap_o, respectively), just before and after the condenser section (Cond_i and Cond_o, respectively), the top center of the loop (TC), and the bottom center of the loop (BC). The average temperatures at the evaporator and the condenser, which are used for thermal resistance calculations, are obtained by taking the average of the temperatures at Evap_i and Evap_o, and Cond_i and Cond_o, respectively. Pressure is recorded at the TC, BC, Cond_i, Cond_o, and center of the evaporator.

The geometry was constructed and meshed using the ANSYS Workbench geometry and mesh applications. The fluid region is meshed with 40,909 elements (Mesh1). The model was also meshed with 85,104 elements (Mesh2) to test grid-independence for temperature and pressure. The average condenser temperature and average evaporator temperature are plotted in Figure 3*a*, and average pressure is plotted in Figure 3*b* for each mesh for a simulation with 90% liquid R134a, relative to total volume, and a 200 W heat input to the evaporator.

As seen in Figure 3*a*, the average evaporator and condenser temperature follows the same trend for each mesh. The average evaporator temperature is very similar for both meshes, and the average condenser temperature is slightly less for Mesh2 than Mesh1. The average pressure follows the same trend for Mesh1 and Mesh2, the average pressure for Mesh2 is slightly lower than that of Mesh1. The TC, BC, average evaporator, and average condenser temperatures and average pressure were monitored for each mesh for a simulation modeled with 90% liquid R134a fill ratio with respect to total loop volume and a 200 W heat input.

Steady-state values are listed in Table 1, along with the percent difference between the two meshes.

As seen in Table 1, the maximum percent difference in temperature is 1.10% between the two meshes, and the percent difference in pressure is 3.30%. These differences and those shown in Figure 3 are small considering the increased computational time of the finer mesh. These minor differences do not justify the increased computational time of using Mesh2, and Mesh1 is used for determination of system temperature and pressure.

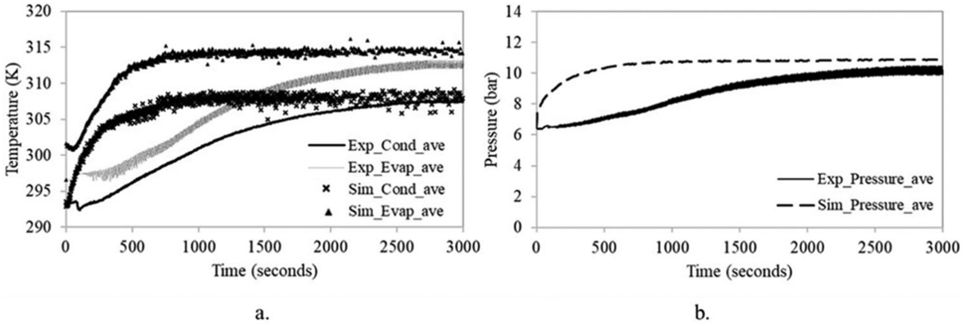

Figure 4. Comparison of experiment and simulation transient response of (a) temperature and (b) pressure to 200 W heat input for 90% Fill Ratio R134a.

A transient simulation with variable time step, with a minimum time step of 0.003 s, is carried out to model the pressure and temperature distribution and the two-phase flow in the TPLTS. The pressure-based, transient, planar solver is used. The flow is modeled as laminar, and the SIMPLE algorithm for pressure-velocity coupling is used. First-order upwind, second-order upwind, and PRESTO schemes are used for the discretization of momentum, energy, and pressure, respectively. Sharp interfaced modeling is used for flow visualization, with Geo-reconstruct discretization for the volume fraction. The sharp model is applicable when there is a distinct interface between the two phases (Choosing Volume Fraction Formulation).

3. Simulation validation and comparison to experimental results

3.1. Temperature and pressure response

The CFD model is validated with experimental data obtained in a previous effort [38]. The simulation was run with fill ratios of 95%, 90%, and 85% liquid R134a with respect to the total loop volume, and heat flux at the evaporator corresponding to a 200, 250, or 300 W heat input. To compare simulation results to experimental results, the average evaporator and condenser temperature and average system pressure are plotted for the simulation and experiment for the 90% fill ratio and 200 W heat input and are shown in Figure 4. The steady-state values for the temperatures around the loop, average pressure, and temperature drop are listed in Table 2 along with the percent difference between the experiment and simulation values for the different fill ratio and heat input simulations.

As seen in Figure 4, temperature and pressure in the simulation reach steady state faster than in the experiment. This is because the heating element used at the evaporator section to supply a constant heat flux takes time to reach that constant heat flux, whereas in the simulation the heat flux is constant throughout the simulation. While the simulation takes less time to reach steady state, the trend in temperature and pressure response is similar to the experiment.

Simulation and experiment average evaporator and condenser temperature and average system pressure are also compared for 95% fill ratio and 200 W heat input conditions and plotted in Figure 5. The steady-state values for the temperatures around the loop, average pressure, and temperature drop are listed in Table 2 along with the percent difference between the experiment and simulation values for the different fill ratio and heat input simulations.

Similar to the 90% fill ratio and 200 W heat input conditions shown in Figure 4, the temperature and pressure in the simulation reach steady state faster than in the experiment for the conditions shown in Figure 5. The temperatures are slightly higher in the simulation than in the experiment due to assumptions made while calculating boundary conditions. Since the

Table 2. Comparison of simulation and experiment steady-state temperatures, pressure, and temperature drop for 95%, 90%, and 85% R134a fill ratio and 200, 250, and 300 W heat input.

Fill ratio	Heat input		Pressure (bar)	TC (K)	BC (K)	Evaporator (K)	Condenser (K)	Temp. drop (K)
95%	200 W	Experiment	8.94	307.43	303.61	308.50	305.09	3.41
		Simulation	11.00	314.59	309.99	313.74	309.80	3.94
		% Difference	18.76	2.28	2.06	1.67	1.51	13.45
90%	200 W	Experiment	10.17	312.25	306.06	312.57	307.46	5.11
		Simulation	10.79	312.99	310.11	314.18	307.92	6.27
		% Difference	5.75	0.24	1.31	0.51	0.15	18.50
	250 W	Experiment	10.82	314.21	308.75	316.22	311.13	5.10
		Simulation	11.94	318.97	313.29	318.08	313.15	4.93
		% Difference	9.40	1.49	1.45	0.58	0.64	3.45
	300 W	Experiment	12.30	318.29	313.46	321.46	315.06	6.40
		Simulation	13.30	323.75	317.94	323.22	317.80	5.41
		% Difference	7.53	1.69	1.41	0.54	0.86	18.30
85%	200 W	Experiment	8.69	306.81	302.08	308.28	303.89	4.39
		Simulation	10.55	316.06	310.22	315.74	311.11	4.63
		% Difference	17.63	2.93	2.63	2.36	2.31	5.18
	250 W	Experiment	9.80	311.07	306.44	313.46	308.64	4.82
		Simulation	11.86	320.77	314.03	320.83	315.41	5.42
		% Difference	17.33	3.02	2.42	2.29	2.14	11.07
	300 W	Experiment	11.38	316.46	311.49	319.96	313.66	6.30
		Simulation	13.24	325.72	317.77	325.72	318.94	6.17
		% Difference	14.06	2.84	1.98	1.59	1.64	2.11

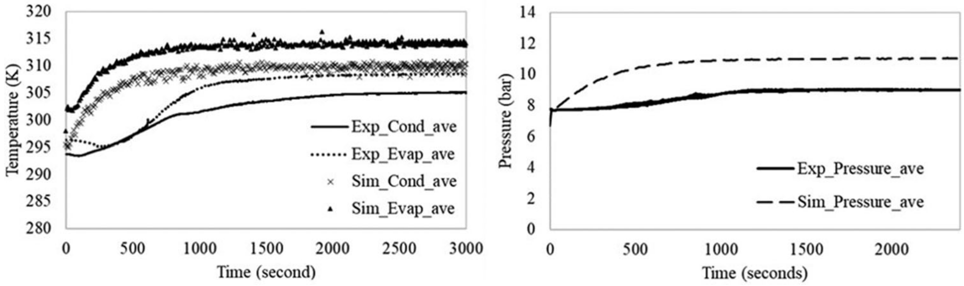

Figure 5. Comparison of experiment and simulation transient response of (a) temperature and (b) pressure to 200 W heat input for 95% fill ratio R134a.

temperature and pressure are related in the simulation, the simulation pressure is also higher than the experiment pressure.

Table 2 lists the steady-state temperatures, average pressure, and temperature drop for simulations and experiments with fill ratios of 95%, 90%, and 85% and heat inputs of 200, 250, and 300 W, and the percent difference between them. The 95% fill ratio was only modeled with a 200 W heat input, as the experiment was only able to reach steady state at a maximum heat input of 200 W without exceeding maximum allowable temperature.

As seen in Table 2, the maximum percent difference in steady-state temperature between the simulation and experiment for the conditions modeled is 3.02% for the 85% fill ratio 250 W heat input conditions, and the maximum percent difference in average pressure is 18.76% for the 95% fill ratio 200 W heat input conditions. Simulation temperature is generally higher than the experiment with corresponding conditions, most likely due to a greater amount of heat being lost to the environment in the experiment than in the simulation. The pressure in the simulations is higher than in the experiments with corresponding heat input and fill ratio conditions due to the higher simulation temperatures. The temperature and pressure are related in the simulation and a higher temperature results in higher pressure. While the system temperature and pressure are generally higher in the simulation than the experiment, the simulation still gives a good

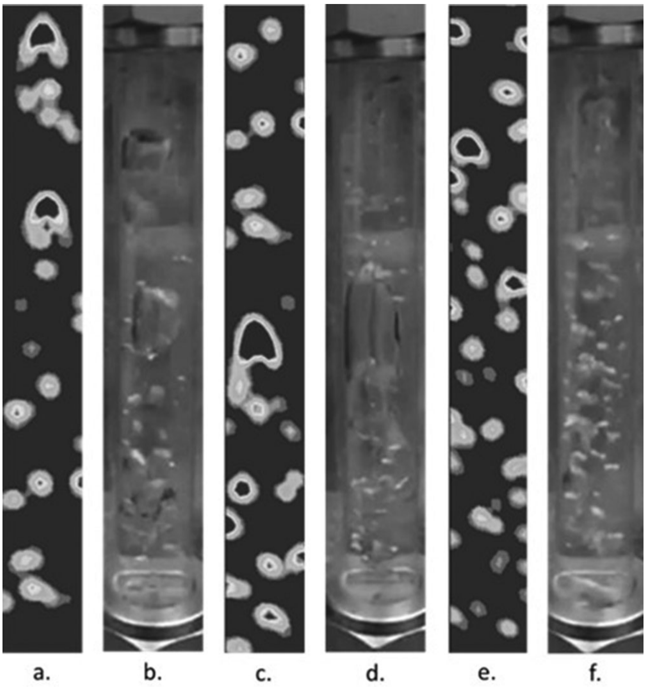

Figure 6. Time evolution of flow visualization at startup of simulation as time progresses from a to c to e, and experiment as time progresses from b to d to f. After bubbles begin to appear in window 1 for 90% R134a fill ratio and 200 W heat input.

approximation of steady-state temperatures and pressure and the trend in response to a heat input, as shown in Figures 4 and 5.

The maximum percent difference for temperature drop for the simulations listed in Table 2, 18.50% for the 90% fill ratio 200 W heat input conditions, is most likely due to the assumptions made during heat flux calculations. After performing error propagation, the experimental uncertainty in temperature drop between the evaporator and condenser is 0.59 K. The simulation temperature drop is within this uncertainty for four of the seven simulations listed in Table 2. While the percent difference in temperature drop is higher than the steady-state system temperature and pressure, there is still a reasonably good agreement between the simulation and experiment.

3.2. Flow visualization

The flow patterns for the liquid and vapor within the TPLTS were compared between the experiment and simulation. To visualize the flow patterns in the experiment, three 5-inch borosilicate glass tubes were added at different locations around the loop, as shown in Figure 2. Figure 6 shows the flow visualization during the startup period in window 1 for the simulation and experiment. Figure 7 shows the flow visualization during the startup of the simulation and experiment in window 2. Flow visualization at window 3 is not shown for any of the fill ratio and heat input conditions discussed below because it remains a liquid throughout the simulation and experiment for the 90% and 95% fill ratios. Similar trends can be observed in flow visualization at the beginning of the experiment and simulation as shown in Figures 6 and 7.

In Figures 6*a*, *b* there are two larger bubbles followed by several smaller bubbles. Then, in Figures 6*c*, *d*, the distance between larger bubbles increases so that only one larger bubble is seen in the window. The larger bubble grows slightly in size and is preceded and followed by a series of smaller bubbles. Next, a section of many small bubbles appears in window 1, as seen in

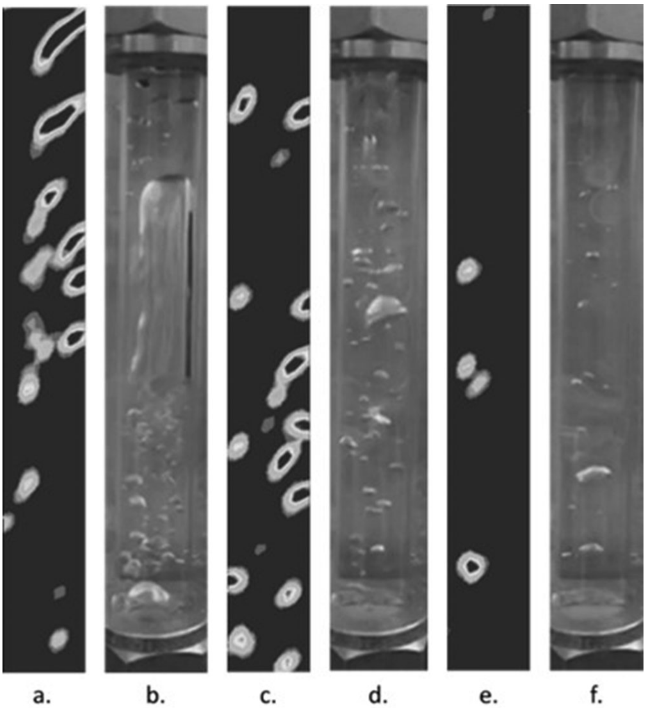

Figure 7. Time evolution of flow visualization at startup of simulation as time progresses from a to c to e, and experiment as time progresses from b to d to f. After bubbles begin to appear in window 2 for 90% R134a fill ratio and 200 W heat input.

Figures 6*e, f*. During startup, the simulation can model the flow patterns in window 1. Figure 6*c* shows the liquid starting to boil at positions where the liquid temperature at the wall is greater than the saturation temperature, which results in continuous nucleation. Vapor bubbles form at these locations and rise through window 2, as shown in Figure 7, to the top of the liquid region where they break and release their vapor content at the top of the loop.

In Figure 7*a*, there are several large bubbles, followed by several small bubbles. However, in Figure 7*b*, there is one large bubble that fills approximately half the visible section of window 2 followed by several smaller bubbles. The simulation does not predict the very large bubble that is seen in Figure 7*b*. Then, in Figures 7*c, d* after the large vapor bubble passes through the window, there is a period of smaller bubbles flowing through window 2. Next, there is a time where only a few small bubbles appear in window 2, as seen in Figures 7*e, f*. The simulation can model the flow patterns in window 2 reasonably well during the startup period of the experiment, except the simulation is not able to produce the larger bubbles that fill most of the window.

Flow patterns were also observed at steady state for the simulation and experiment. Figure 8 shows the flow through the simulation and experiment at steady state just after the evaporator section. As seen in Figure 8, there are a series of smaller bubbles flowing through window 1 at steady state. The location of the bubbles appears random in both the simulation and the experiment, and the bubbles sizes are relatively small. The simulation gives a good representation of the size and frequency of vapor bubbles flowing through window 1 just after the evaporator for these conditions.

The flow-through window 2 at the top right of the loop is also observed for both the simulation and experiment at steady state, and flow patterns are shown in Figure 9. There is a clear pattern in the flow-through window 2 that can be seen in the simulation and experiment. First, a small bubble passes through window 2, as shown in Figures 9*a, b*. A larger bubble follows, as

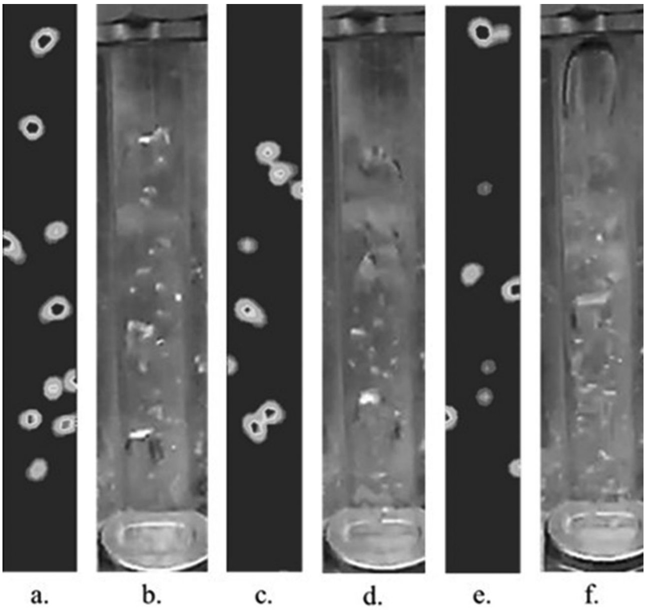

Figure 8. Time evolution of flow visualization at steady state of simulation as time progresses from a to c to e, and experiment as time progresses from b to d to f in window 1 for 90% R134a fill ratio and 200 W heat input.

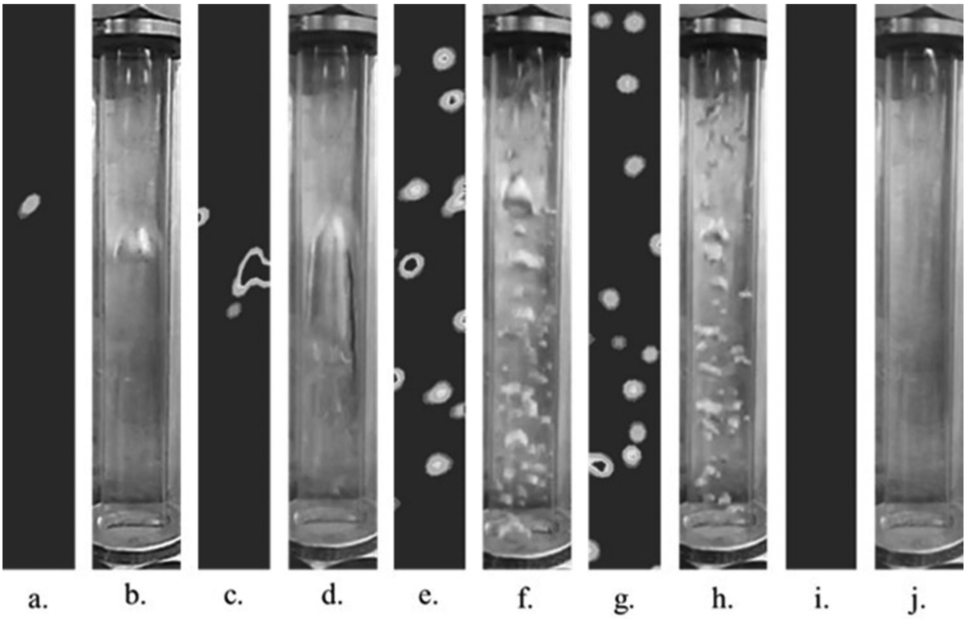

Figure 9. Time evolution of flow visualization at steady state of simulation as time progresses from a to c to e to g to i, and experiment as time progresses from b to d to f to h to j in window 2 for 90% R134a fill ratio and 200 W heat input.

shown in Figures 9*c*, *d*. This larger bubble is followed by a section of fast-moving smaller bubbles which decrease slightly in size, as seen in Figure 9*e*–9*h*. After this section of smaller bubbles, there is a period during which no vapor is present in window 2, as shown in Figures 9*i*, *j*. This process then repeats. As seen in Figure 9, the simulation gives a good representation of the flow

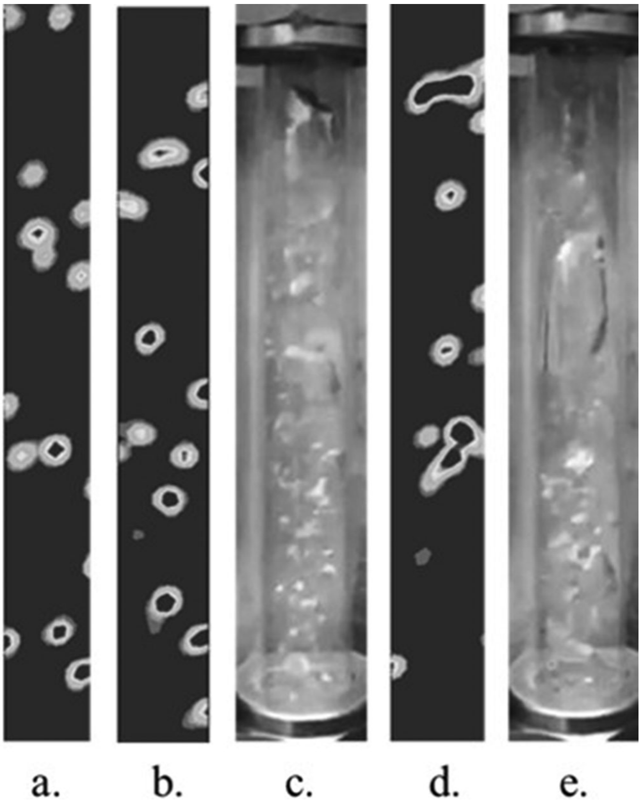

Figure 10. Time evolution of flow visualization at steady state of simulation as time progresses from a to b to d, and experiment as time progresses from c to e in window 1 for 90% R134a fill ratio and 250 W heat input.

patterns through window 2 at steady state and can reproduce the general pattern that is seen in the experiment.

Flow visualization is also studied in the simulation at steady state for the 90% fill ratio and 250 W heat input and compared to experimental data. Figures 10 and 11 show the flow through windows 1 and 2, respectively, for the simulation and experiment with these conditions. It can be seen in Figure 10*c* that the flow through the experiment at window 1 at steady state is a series of small bubbles, followed by a few larger bubbles in Figure 10*e*. This process repeats at window 1 at steady state for these conditions and can also be seen in the simulation. Figures 10*a*, *b* show a series of small bubbles flowing through this section on the model, followed by several larger bubbles in Figure 10*d*, which gives a reasonably good approximation of the size and frequency of the bubbles flowing through window 1 at steady state. Also, when comparing the flow in Figures 8–10 for the 200 and 250 W heat inputs, respectively, at steady state for 90% R134a fill ratios at window 1, it can be seen that the size and frequency of the bubbles in the simulation increases with increasing heat input, as is seen in the experiment.

In Figure 11, the flow pattern in the experiment can be observed as several bubbles flowing through the window (Figure 11*b*) until the frequency decreases and only one bubble flows through the window at a time (Figure 11*d*), and eventually no vapor bubbles are present in window 2 (Figure 11*f*). Then, a larger bubble, followed by several smaller bubbles flows through the window (Figure 11*h*) and the process repeats. This process is represented in the simulation in Figures 11*a*, *c*, *e*, *g*. The simulation gives a reasonably good approximation of the flow pattern for the 90% R134a fill ratio and 250 W heat input conditions.

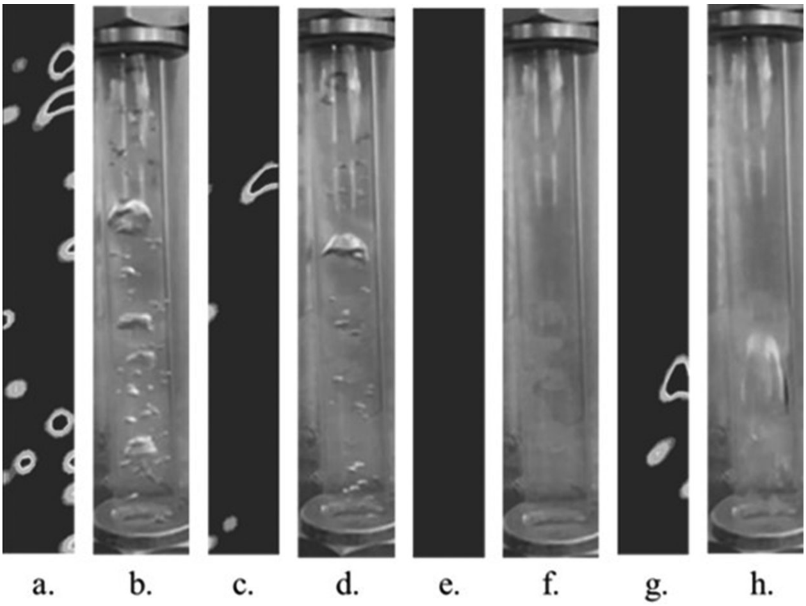

Figure 11. Time evolution of flow visualization at steady state of simulation as time progresses from a to c to e to g, and experiment as time progresses from b to d to f to h in window 2 for 90% R134a fill ratio and 250 W heat input.

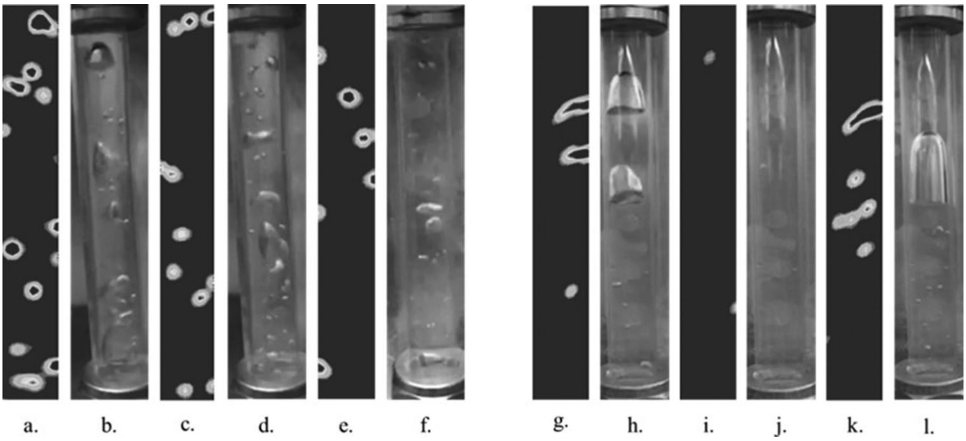

Figure 12. Time evolution of flow visualization at startup of simulation in window 1 as time progresses from a to c to e and window 2 as time progresses from g to i to k, and experiment in window 1 as time progresses from b to d to f and window 2 as time progresses from h to j to l for 95% R134a fill ratio and 200 W heat input.

Flow visualization for the 95% fill ratio 200 W heat input conditions is shown in Figures 12 and 13 at startup and steady state, respectively, for the simulation and experiment. As seen in Figures 12*a*–12*f*, the flow pattern in the simulation follows the same trend as in the experiment where there are a series of several larger bubbles which decrease in size and frequency as time progresses at startup. Figures 12*g*–12*l* shows window 2 at startup, where in the experiment several large bubbles flow through window 2, followed by a time of no bubbles or very small bubbles, then another larger bubble. The simulation can predict this pattern, except is not capable of reproducing the large bubble shown in Figure 12*l*.

Figures 13*a*, *b* show the flow at steady state through window 1 for the 95% R134a fill ratio and 200 W heat input condition, and Figures 13*g*–13*l* show the flow through window 2 at steady

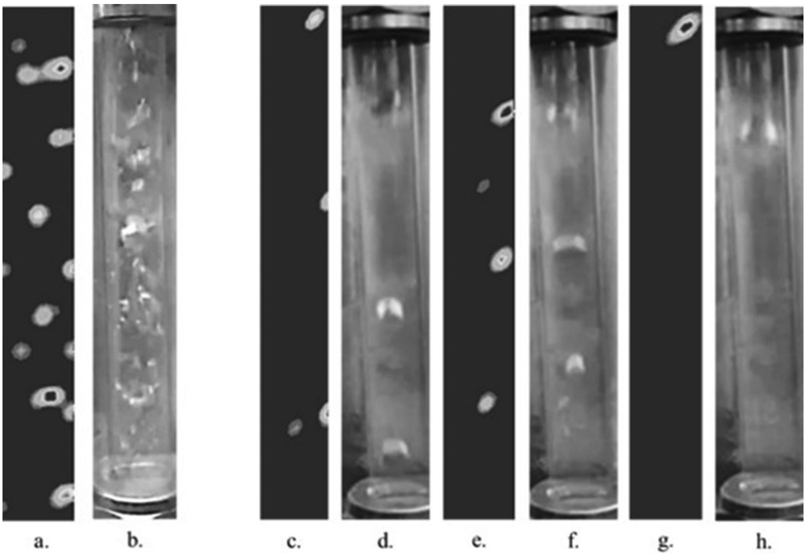

Figure 13. Time evolution of flow visualization at steady state of simulation at (a) window 1 and as time progresses from c to e to g in window 2, and experiment in (b) window 1 and as time progresses from d to f to h in window 2 for 95% R134a fill ratio and 200 W heat input.

state. At steady state for this condition, a series of small bubbles flows continuously through window 1, as seen in Figures 13*a*, *b*. At window 2, several bubbles pass through at varying frequency. At times, there are three vapor bubbles visible in the simulation and experiment at one instant, as shown in Figures 13*c*–13*f*, and sometimes only one vapor bubble is present, as seen in Figures 13*g*–13*h*. It can also be seen when comparing Figures 13–8 for the 95% and 90% fill ratios, respectively, with 200 W heat input that there is a larger amount of vapor present in window 2 for the 90% fill ratio than the 95% fill ratio, as is expected, in the simulation and experiment.

The simulation gives a reasonably good approximation for the flow patterns through windows 1 and 2 of the experiment for a 95% R134a fill ratio and 200 W heat input and a 90% R134a fill ratio with 200 and 250 W heat inputs. However, the simulation is not able to reproduce the larger bubbles that sometimes fill half or more than half the length of window 2.

4. Conclusions

A two-phase closed-loop thermosyphon filled with 85–95% R134a in 5% increments, with respect to the total volume, is considered. A 2-D CFD simulation was developed where flow patterns and temperature and pressure responses can be observed. The proposed CFD model can predict the steady-state temperature and pressure within the TPLTS for the fill ratios and heat inputs studied. The simulation is also able to reproduce the general flow patterns of the liquid and vapor phase working fluid during the startup period and at steady state for these conditions reasonably well, except for the very large bubbles. The proposed CFD model was validated with experimental data.

Funding

This material is based upon work supported by the National Science Foundation under Grant No. 1744118 to the University of Connecticut.

References

[1] A. Faghri, *Heat Pipe Science and Technology*, 2nd ed. Kanpur, Uttar Pradesh: Global Digital Press, 2016.

[2] S. Boothaisong, S. Rittidech, T. Chompookham, M. Thongmoon, Y. Ding, and Y. Li, "Three-dimensional transient mathematical model to predict the heat transfer rate of a heat pipe," *Adv. Mech. Eng.*, vol. 7, no. 2, pp. 168781401456781, Feb. 2015. 10.1177/1687814014567811. [CrossRef]]

[3] A. Faghri, "Heat pipes and thermosyphons," in *Handbook Thermal Science and Engineering*, F. A. Kulacki, Ed. Switzerland: Springer Nature, 2017, pp. 1–50. 10.1007/978-3-319-26695-4_52.

[4] A. Faghri, "Review and advances in heat pipe science and technology," *J. Heat Transf.*, vol. 134, no. 12, pp. 123001, Oct. 2012. DOI: 10.1115/1.4007407.

[5] L. M. Poplaski, A. Faghri, and T. L. Bergman, "Analysis of internal and external thermal resistances of heat pipes including fins using a three-dimensional numerical simulation," *Int. J. Heat Mass Transf.*, vol. 102, pp. 455–469, Nov. 2016. DOI: 10.1016/j.ijheatmasstransfer.2016.05.116.

[6] A. Faghri, "Heat pipes: review, opportunites and challenges," *Front. Heat Pipes*, vol. 5, no. 1, Apr. 2014. DOI: 10.5098/fhp.5.1.

[7] T. L. Bergman and A. Faghri, Review and advances in heat pipe analysis and numerical simulation. In Numerical Simulation of Heat Exchangers, W. J. Minkowycz, E. M. Sparrow, J. P. Abraham, and J. M. Gorman, Eds. Boca Raton, FL, USA: CRC Press, 2017, pp. 173–212. Available: https://uconn.illiad.oclc.org/illiad/illiad.dll?Action=10&Form=75&Value=855746.

[8] Y. J. Park, H. K. Kang, and C. J. Kim, "Heat transfer characteristics of a two-phase closed thermosyphon to the fill charge ratio," *Int. J. Heat Mass Transf.*, vol. 45, no. 23, pp. 4655–4661, Mar. 2002. Available: (02)00169-2. DOI: 10.1016/S0017-9310(02)00169-2.

[9] C. Harley and A. Faghri, "Complete transient two-dimensional analysis of two-phase closed thermosyphons including the falling condensate film," *J. Heat Transf.*, vol. 116, no. 2, pp. 418–426, May 1994. DOI: 10.1115/1.2911414.

[10] H. Shabgard, B. Xiao, A. Faghri, R. Gupta, and W. Weissman, "Thermal characteristics of a closed thermosyphon under various filling conditions," *Int. J. Heat Mass Transf.*, vol. 70, pp. 91–102, Mar. 2014. DOI: 10.1016/j.ijheatmasstransfer.2013.10.053.

[11] A. Faghri and Y. Zhang, Transport phenomena in multiphase systems. Elsevier Academic Press, 2006. Available: https://www.thermalfluidscentral.org/e-books/book-intro.php?b=42.

[12] X. Wang, Y. Wang, H. Chen, and Y. Zhu, "A combined CFD/visualization investigation of heat transfer behaviors during geyser boiling in two-phase closed thermosyphon," *Int. J. Heat Mass Transf.*, vol. 121, pp. 703–714, Jun. 2018. DOI: 10.1016/j.ijheatmasstransfer.2018.01.005.

[13] A. Alizadehdakhel, M. Rahimi, and A. A. Alsairafi, "CFD modeling of flow and heat transfer in a thermosyphon," *Int. Commun. Heat Mass Transf.*, vol. 37, no. 3, pp. 312–318, Mar. 2010. DOI: 10.1016/j.icheatmasstransfer.2009.09.002.

[14] B. Fadhl, L. C. Wrobel, and H. Jouhara, "Numerical modelling of the temperature distribution in a two-phase closed thermosyphon," *Appl. Ther. Eng.*, vol. 60, no. 1–2, pp. 122–131, Oct. 2013. DOI: 10.1016/j.applthermaleng.2013.06.044.

[15] H. Jouhara, B. Fadhl, and L. C. Wrobel, "Three-dimensional CFD simulation of geyser boiling in a two-phase closed thermosyphon," *Int. J. Hydrogen Energy*, vol. 41, no. 37, pp. 16463–16476, Oct. 2016. DOI: 10.1016/j.ijhydene.2016.02.038.

[16] Z. Xu, Y. Zhang, B. Li, and J. Huang, "Modeling the phase change process for a two-phase closed thermosyphon by considering transient mass transfer time relaxation parameter," *Int. J. Heat Mass Transf.*, vol. 101, pp. 614–619, Oct. 2016. DOI: 10.1016/j.ijheatmasstransfer.2016.05.075.

[17] Y. Naresh and C. Balaji, "Thermal performance of an internally finned two phase closed thermosyphon with refrigerant R134a: a combined experimental and numerical study," *Int. J. Ther. Sci.*, vol. 126, pp. 281–293, Apr. 2018. DOI: 10.1016/j.ijthermalsci.2017.11.033.

[18] L. Zou and W. Wang, "Simulation study of flow and heat transfer in a thermosyphon," *Numer. Heat Transf. B*, vol. 72, no. 1, pp. 55–70, Jun. 2017. DOI: 10.1080/10407790.2017.1338098.

[19] P. Zhang, B. Wang, W. Shi, L. Han, and X. Li, "Modeling and performance analysis of a two-phase thermosyphon loop with partially/fully liquid-filled downcomer," *Int. J. Refriger.*, vol. 58, pp. 172–185, Oct. 2015. DOI: 10.1016/j.ijrefrig.2015.06.014.

[20] R. Khodabandeh, "Pressure drop in riser and evaporator in an advanced two-phase thermosyphon loop," *Int. J. Refriger.*, vol. 28, no. 5, pp. 725–734, Aug. 2005. DOI: 10.1016/j.ijrefrig.2004.12.003.

[21] S.-W. Kang, M.-C. Tsai, C.-S. Hsieh, and J.-Y. Chen, "Thermal performance of a loop thermosyphon," *Tamkang J. Sci. Eng.*, vol. 13, no. 3, pp. 281–288, 2010. Available: http://www2.tku.edu.tw/~tkjse/13-3/07-ME9707.pdf.

[22] R. T. Dobson and J. C. Ruppersberg, "Flow and heat transfer in a closed loop thermosyphon. Part I – theoretical simulation," *J. Energy Southern Afr.*, vol. 18, no. 4, pp. 32–40, Nov. 2017. Available: http://www.erc.uct.ac.za/sites/default/files/image_tool/images/119/jesa/18-4jesa-dobson.pdf.

[23] S. H. Park, Y. S. Kim, S. Y. Kim, Y. G. Park, and M. Y. Ha, "Numerical study on the two-phase flow pattern and temperature distribution in a loop thermosyphon as a defrost device at the evaporator in the refrigerator," *J. Mech. Sci. Technol.*, vol. 32, no. 12, pp. 5927–5936, Dec. 2018. DOI: 10.1007/s12206-018-1144-2.

[24] P. Zhang, B. Wang, W. Shi, and X. Li, "Experimental investigation on two-phase thermosyphon loop with partially liquid-filled downcomer," *Appl. Energy*, vol. 160, pp. 10–17, Dec. 2015. DOI: 10.1016/j.apenergy.2015.09.033.

[25] N. Z. Aung and S. Li, "Numerical investigation on effect of riser diameter and inclination on system parameters in a two-phase closed loop thermosyphon solar water heater," *Energy Conversion Manage.*, vol. 75, pp. 25–35, Nov. 2013. DOI: 10.1016/j.enconman.2013.06.001.

[26] S. Bodjona, E. Videcoq, R. Saurel, A. Chinnayya, A. M. Benselama, and Y. Bertin, "Transient simulation a two-phase loop thermosyphon a model out thermodynamic equilibrium," *Int. J. Heat Mass Transf.*, vol. 108, pp. 2321–2332, May 2017. DOI: 10.1016/j.ijheatmasstransfer.2017.01.061.

[27] S. Bodjona, M. Girault, E. Videcoq, and Y. Bertin, "Reduced order model of a two-phase loop thermosyphon by modal identification method," *Int. J. Heat Mass Transf.*, vol. 123, pp. 637–654, Aug. 2018. DOI: 10.1016/j.ijheatmasstransfer.2018.02.075.

[28] D. Lu, X. Zhang, and C. Guo, "Stability analysis for single-phase liquid metal rectangular natural circulation loops," *Ann. Nucl. Energy*, vol. 73, pp. 189–199, Nov. 2014. DOI: 10.1016/j.anucene.2014.06.014.

[29] M. Maiani, W. J. M. de Kruijf, and W. Ambrosini, "An analytical model for the determination of stability boundaries in a natural circulation single-phase thermosyphon loop," *Int. J. Heat Fluid Flow*, vol. 24, no. 6, pp. 853–863, Dec. 2003. DOI: 10.1016/j.ijheatfluidflow.2003.07.002.

[30] P. K. Vijayan, "Experimental observations on the general trends of the steady state and stability behaviour of single-phase natural circulation loops," *Nucl. Eng. Des.*, vol. 215, no. 1–2, pp. 139–152, Jun. 2002. Available:(02)00047-X. DOI: 10.1016/S0029-5493(02)00047-X.

[31] E. A. Burroughs, E. A. Coutsias, and L. A. Romero, "A reduced-order partial differential equation model for the flow in a thermosyphon," *J. Fluid Mech.*, vol. 543, no. 1, pp. 203–237, Nov. 2005. DOI: 10.1017/S0022112005006361.

[32] D. S. Pilkhwal, W. Ambrosini, N. Forgione, P. K. Vijayan, D. Saha, and J. C. Ferreri, "Analysis of the unstable behaviour of a single-phase natural circulation loop with one-dimensional and computational fluid-dynamic models," *Ann. Nucl. Energy*, vol. 34, no. 5, pp. 339–355, May. 2007. DOI: 10.1016/j.anucene.2007.01.012.

[33] K. Naveen, K. N. Iyer, J. B. Doshi, and P. K. Vijayan, "Investigations on single-phase natural circulation loop dynamics. Part 3: role of expansion tank," *Prog. Nucl. Energy*, vol. 78, pp. 65–79, 2015. DOI: 10.1016/j.pnucene.2014.08.007.

[34] M. M. Farawila, D. R. Todd, M. J. Ades José, and N. N. Reyes, "Analytical stability analogue for a single-phase natural-circulation loop," *Nucl. Sci. Eng.*, vol. 184, no. 3, pp. 321–333, Nov. 2016. DOI: 10.13182/NSE16-24.

[35] L. Luzzi *et al.*, "Assessment of analytical and numerical models on experimental data for the study of single-phase natural circulation dynamics in a vertical loop," *Chem. Eng. Sci.*, vol. 162, pp. 262–283, Apr. 2017. DOI: 10.1016/j.ces.2016.12.058.

[36] H. Cheng, H. Lei, and C. Dai, "Thermo-hydraulic characteristics and second-law analysis of a single-phase natural circulation loop with end heat exchangers," *Int. J. Ther. Sci.*, vol. 129, pp. 375–384, Jul. 2018. DOI: 10.1016/j.ijthermalsci.2018.03.026.

[37] R. B. Bejjam and K. Kiran Kumar, "Numerical investigation to study the effect of loop inclination angle on thermal performance of nanofluid-based single-phase natural circulation loop," *Int. J. Ambient Energy Int.*, vol. 40, pp. 885–893, Mar. 2018. DOI: 10.1080/01430750.2018.1432502.

[38] S. Kloczko, A. Faghri, and Y. Li, "Is a non-phase change heat pipe a new heat pipe?" *Int. J. Heat Mass Transf.*, vol. 145, pp. 118676, Dec. 2019. DOI: 10.1016/j.ijheatmasstransfer.2019.118676.

[39] Volume of Fluid (VOF) Model Theory. Release 12.0 © ANSYS, Inc. Jan. 2009. Available: https://www.sharcnet.ca/Software/Fluent6/html/ug/node880.htm. Accessed January 28, 2018.

[40] F. Dong, Z. Wang, T. Cao, and J. Ni, "A novel interphase mass transfer model toward the VOF simulation of subcooled flow boiling," *Numer. Heat Transf. A.*, vol. 76, no. 4, pp. 220–231, Mar. 2019. DOI: 10.1080/10407782.2019.1627838.

[41] Thermophysical Properties of Fluid Systems, National Institute of Standards and Technology, 2017. Available: http://webbook.nist.gov/chemistry/fluid/. Accessed January 4, 2018.

[42] W. H. Lee, "A pressure iteration scheme for two-phase flow modeling," *Multiphase Transport Fundamentals, Reactor Safety, Applications*, vol. 1, pp. 407–431, 1980. Available: http://www.newsmth.net/

bbsanc.php?path=%2Fgroups%2Fsci.faq%2FMechanics%2FNews%2FNetF%2Fsolid%2FM.1284776945.E0&ap=173276.

[43] D. Sun, J. Xu, and Q. Chen, "Modeling of the evaporation and condensation phase-change problems with fluent," *Numer. Heat Transf. B*, vol. 66, no. 4, pp. 326–342, Jan. 2014. DOI: 10.1080/10407790.2014.915681.

[44] Y. Kim, J. Choi, S. Kim, and Y. Zhang, "Effects of mass transfer time relaxation parameters on condensation in a thermosyphon," *J. Mech. Sci. Technol.*, vol. 29, no. 12, pp. 5497–5505, Dec. 2015. DOI: 10.1007/s12206-015-1151-5.

[45] J.U. Brackbill, D.B. Kothe, and D.B. Kothe, "A continuum method for modeling surface tension. *J. Comput. Phys.*, vol. 100, no. 2, pp. 335–354, Jul. 1992. Available:(92)90240-Y. DOI: 10.1016/0021-9991(92)90240-Y.